J. Appl. Numer. Optim. 7 (2025), No. 3, pp. 377-398 Available online at http://jano.biemdas.com https://doi.org/10.23952/jano.7.2025.3.06

SHAPES OPTIMISING GRAND RESISTANCE TENSOR ENTRIES FOR A RIGID BODY IN A STOKES FLOW

CLÉMENT MOREAU^{1,*}, KENTA ISHIMOTO², YANNICK PRIVAT^{3,4}

¹Nantes Université, École Centrale Nantes, CNRS, LS2N, UMR 6004, F-44000 Nantes, France

²Department of Mathematics, Kyoto University, Japan

³Université de Lorraine, CNRS, Inria, IECL, F-54000 Nancy, France

⁴Institut Universitaire de France (IUF), France

In honor of Professor Tamás Terlaky's 70th birthday

Abstract. We investigate the optimal shapes for the hydrodynamic resistance of a rigid body set in motion in a Stokes flow. At this low Reynolds number regime, the hydrodynamic drag properties of an object are encoded in a finite number of parameters contained in the grand resistance tensor. Considering these parameters as objective functions, we use calculus of variations techniques to derive a general shape derivative formula, allowing to specify how to deform the body shape to improve the objective value of any given resistance tensor entry. We then describe a practical algorithm for numerically computing the optimized shapes and apply it to several examples. Numerical results reveal interesting new geometries for various criteria and perspectives into optimal hydrodynamic profiles.

Keywords. Augmented Lagrangian algorithm; Hadamard boundary variation method; Hydrodynamic resistance; Low-Reynolds-number flows; Shape optimisation.

2020 Mathematics Subject Classification, 76D55, 76M45, 93B05.

1. Introduction

The interaction between solid objects and a surrounding fluid is at the heart of many fluid mechanics problems stemming from various fields such as physics, engineering and biology. Among other factors, the behaviour of such fluid-structure interaction systems is predominantly determined by the boundary conditions at the surface of the solid, but also by the geometry of the solid itself, commonly called its shape. In this context, the research for some notion of shape optimality in the fluid-structure interaction is widespread, with the objective of understanding which shapes allow for optimal response from the fluid, typically involving energy-minimising criteria [37].

At low Reynolds number, a regime occurring in particular at the microscopic scale where viscosity dominates on inertial effects, fluid dynamics are governed by the Stokes equations. These equations are linear and time-reversible – a remarkable specificity compared to the more

E-mail address: clement.moreau@ls2n.fr (C. Moreau).

Received 20 September 2025; Accepted 4 November 2025; Published online 24 November 2025.

©2025 Journal of Applied and Numerical Optimization

^{*}Corresponding author.

general Navier-Stokes equations, which makes fluid-structure interaction and locomotion at microscopic scale a peculiar world [44].

In particular, when considering the *resistance problem* of a rigid body moving into a fluid in the Stokes regime, a linear relationship holds between the motion of a body (translation and rotation) and the effects (forces and torques) it experiences. This relationship is materialised by the well-known *grand resistance tensor*.

Remarkably, once a reference frame is fixed, the grand resistance tensor is determined solely by the object's geometry and not by its instantaneous motion, provided the conditions at infinity (or the outer boundary) are treated consistently. In other words, for an incompressible Newtonian fluid in the Stokes regime (at low Reynolds number) with fixed viscosity, the hydrodynamic resistance properties of a rigid body are intrinsic to its shape. The question of which shapes possess maximal or minimal values for these resistance parameters then naturally arises, both from a theoretical fluid mechanics perspective, and as potential ways to explain the sometimes intriguing geometries of microorganisms [34, 47, 53, 58].

Optimal shapes for resistance problems have been addressed in previous studies. In particular, the minimal drag problem, which seeks the shape of fixed volume opposing the least hydrodynamic resistance to translation in a set direction, is well known and was solved in the 1970s, both analytically [42] and numerically [3]. The characteristic rugby-ball shape resulting from this optimisation problem has then been used as a reference for many later works, among which we can cite the adaptations to two-dimensional and axisymmetric flows in [46, 49], linear elastic medium in [59], or minimal drag for fixed surface in [36]. These studies rely on symmetry properties for the minimal drag problem, and such methods fail to be immediately extended to solve the optimisation of the generic resistance problem, associated with other entries of the resistance tensor.

Shape optimisation in microhydrodynamics has also been widely carried out in the context of microswimmer locomotion. Notable works include [45], where the best pitch and cross-section for efficient magnetic swimmers is numerically and experimentally discussed, and [5, 18, 27], where parametric optimisation is conducted to find the best geometry for flagellated microswimmers. Efficient shapes for periodic swimming strokes and ciliary locomotion are addressed in [13, 52].

However, in these studies, restrictive assumptions are made on the possible shapes, with the optimisation being carried on a few geometrical parameters and not on a general space of surfaces in 3D. Another approach, allowing to explore a wider class of shapes than with parametric optimisation, is based on the use of shape derivatives: a generalisation of the notion of derivative, which yields a perturbation function of a domain in a descent direction [15, 23, 54]. However, this method requires caution regarding the regularity assumptions on the boundaries of the domains involved [20]. Other popular methods for shape optimisation in structural mechanics include density methods, in which the characteristic function of a domain is replaced by a density function – we mention in particular the celebrated SIMP method [7, 9, 17], and the level set method, [1, 40, 50, 57] which can handle changes of topology. Obtaining efficient numerical algorithms to apply these analytical methods to find optimal shapes is also challenging: one must be able to handle both a decrease of the objective function, while avoiding that the numerical representation becomes invalid (for example because of problems related to the mesh or to changes in the topology of the shapes considered).

In the context of low-Reynolds number fluid mechanics, variational techniques and shape derivatives are used in [6, 21, 35] to optimize deforming axisymmetric microswimmers. In [33, 56], the authors carry the optimisation of the torque-speed mobility coefficient in the context of magnetically propelled swimmers, for a shape constrained to be a slender curved body, yielding helicoidal folding. The shape variation is introduced for a general shape functional in [56], before focusing on shapes characterised by a one-dimensional curve, and a single entry of the resistance tensor. The present study follows analogous ideas to establish a systematic theoretical and numerical study of the coefficients of the grand resistance tensor, including some of the extradiagonal coefficients which, to the best of the authors' knowledge, have not been tackled in previous studies.

Hence, as the principal aim of this paper, we will provide a general framework of shape optimisation for this type of problem, and show that the optimisation of any entry of the resistance tensor amounts to a single, simple formula for the shape derivative, which depends on the solution of two Stokes problems whose boundary conditions depend on the considered entry. We then describe an algorithm to numerically implement the shape optimisation and display some illustrative examples.

2. PROBLEM STATEMENT

2.1. Resistance problem for a rigid body in Stokes flow. We consider a rigid object set in motion into an incompressible fluid with viscosity μ at zero Reynolds number, with coordinates \mathbf{x} expressed in the fixed lab frame $(O, \mathbf{e}_1, \mathbf{e}_2, \mathbf{e}_3)$, as shown on the left panel of Fig. 1. The object's surface is denoted by \mathcal{S} and we assume that the fluid is contained in a bounded domain \mathcal{B} , thus occupying a volume \mathcal{V} having $\partial \mathcal{V} = \mathcal{S} \cup \partial \mathcal{B}$ as boundary. We assume that the outer boundary $\partial \mathcal{B}$ is sufficiently far from the object so that its influence on the hydrodynamic resistance can be expected to be negligible.

At the container boundary $\partial \mathcal{B}$, we consider a uniform, linear background flow U^{∞} , broken down into translational velocity vector \mathbf{Z}^{∞} , rotational velocity vector $\mathbf{\Omega}^{\infty}$ and rate-of-strain (second-rank) tensor \mathbf{E}^{∞} components as follows:

$$\boldsymbol{U}^{\infty} = \mathbf{Z}^{\infty} + \boldsymbol{\Omega}^{\infty} \times \boldsymbol{x} + \boldsymbol{E}^{\infty} \boldsymbol{x}. \tag{2.1}$$

Similarly, the object's rigid motion velocity field, assumed to be without slip, is simply described by

$$U = Z + \Omega \times x, \tag{2.2}$$

with U and Ω denoting its translational and rotational velocities. Having set as such the velocities at the boundary of $\mathscr V$ defines a boundary value problem for the fluid velocity field u and pressure field p, which satisfy the Stokes equations:

$$\begin{cases}
\mu \Delta \mathbf{u} - \nabla p = \mathbf{0} & \text{in } \mathcal{V}, \\
\nabla \cdot \mathbf{u} = 0 & \text{in } \mathcal{V}, \\
\mathbf{u} = \mathbf{U} & \text{on } \mathcal{S}, \\
\mathbf{u} = \mathbf{U}^{\infty} & \text{on } \partial \mathcal{B}.
\end{cases} \tag{2.3}$$

From the solution of this Stokes problem with set boundary velocity, one can then calculate the hydrodynamic drag (force \mathbf{F}^h and torque \mathbf{T}^h) exerted by the moving particle to the fluid, via the

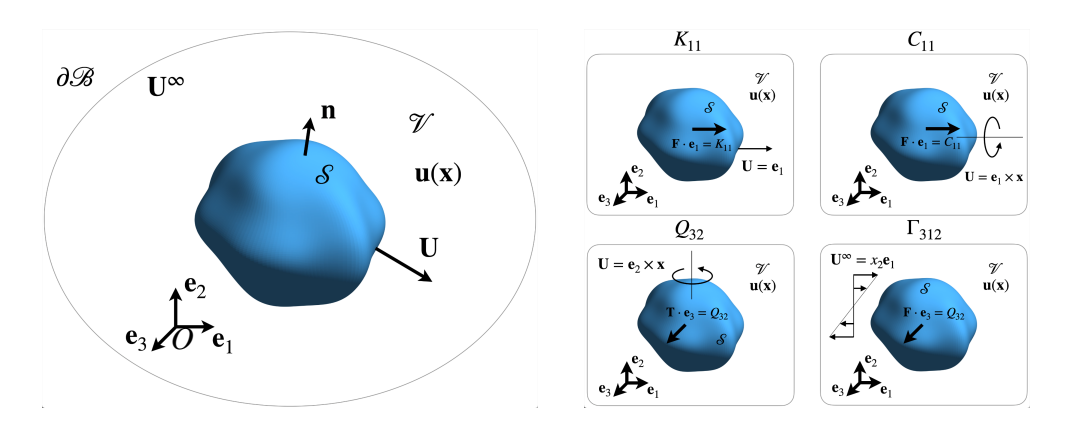


FIGURE 1. Problem setup: a rigid body in a Stokes flow. A diagram of the general Stokes problem (2.3) can be seen on the left of the figure. The panels on the right-hand side show examples of resistance problems associated to selected entries of the grand resistance tensor. For instance, for K_{11} (top left), one sets the motion of the object to a unitary translation in the direction e_1 , and then K_{11} may be obtained as the component along e_1 of the total drag force F exerted on the object. The other coefficients shown on the other panels are analogously obtained by using the appropriate boundary conditions and drag force or torque shown on the figure.

following surface integrals formulae over \mathscr{S} :

$$\mathbf{F}^{h} = -\int_{\mathscr{L}} \boldsymbol{\sigma}[\mathbf{u}, p] \mathbf{n} d\mathscr{S}, \tag{2.4}$$

$$\mathbf{T}^{h} = -\int_{\mathscr{D}} \mathbf{x} \times (\boldsymbol{\sigma}[\mathbf{u}, p]\mathbf{n}) \, d\mathscr{S}. \tag{2.5}$$

In (2.4)-(2.5), \mathbf{n} is the normal to $d\mathcal{S}$ pointing outward to the body (see Fig. 1), and $\boldsymbol{\sigma}$ is the stress tensor, defined as $\boldsymbol{\sigma}[\boldsymbol{u},p] = -p\boldsymbol{I} + 2\mu\boldsymbol{e}[\boldsymbol{u}]$, in which \boldsymbol{I} denotes the identity tensor and $\boldsymbol{e}[\boldsymbol{u}]$ is the rate-of-strain tensor, given by

$$\boldsymbol{e}[\boldsymbol{u}] = \frac{1}{2} \left(\nabla \boldsymbol{u} + (\nabla \boldsymbol{u})^T \right).$$

Finding this way the hydrodynamic drag for a given velocity field is called the *resistance problem* – as opposed to the *mobility problem* in which one seeks to find the velocity generated by a given force and torque profile on the boundary.

2.2. **Grand resistance tensor.** In addition to Equations (2.4)-(2.5), a linear relationship between $(\mathbf{F}^h, \mathbf{T}^h)$ and $(\mathbf{U}, \mathbf{U}^\infty)$ can be derived from the linearity of the Stokes equation (see [32, Chapter 5]):

$$\begin{pmatrix} \mathbf{F}^{h} \\ \mathbf{T}^{h} \\ \mathbf{S} \end{pmatrix} = \mathbf{R} \begin{pmatrix} \mathbf{Z} - \mathbf{Z}^{\infty} \\ \mathbf{\Omega} - \mathbf{\Omega}^{\infty} \\ -\mathbf{E}^{\infty} \end{pmatrix} = \begin{pmatrix} \mathbf{K} & \mathbf{C} & \mathbf{\Gamma} \\ \tilde{\mathbf{C}} & \mathbf{Q} & \mathbf{\Lambda} \\ \tilde{\mathbf{\Gamma}} & \tilde{\mathbf{\Lambda}} & \mathbf{M} \end{pmatrix} \begin{pmatrix} \mathbf{Z} - \mathbf{Z}^{\infty} \\ \mathbf{\Omega} - \mathbf{\Omega}^{\infty} \\ -\mathbf{E}^{\infty} \end{pmatrix}.$$
(2.6)

The stresslet S, defined as

$$\mathbf{S} = \frac{1}{2} \int_{\mathscr{S}} (\mathbf{x} \cdot \boldsymbol{\sigma}[\mathbf{u}, p] \mathbf{n}^T + \boldsymbol{\sigma}[\mathbf{u}, p] \mathbf{n} \cdot \mathbf{x}^T) d\mathscr{S},$$

appears on the right-hand side of Equation (2.6) and is displayed here for the sake of completeness, though we will not be dealing with it in the following.

The tensor R, called the grand resistance tensor, is symmetric and positive definite. As seen in Equation (2.6), it may be written as the concatenation of nine tensors, each accounting for one part of the force-velocity coupling. The second-rank tensors K and C represents the coupling between hydrodynamic drag force and, respectively, translational and rotational velocity. Similarly, \tilde{C} and Q are second-rank tensors coupling hydrodynamic torque with translational and rotational velocity. Note that, by symmetry of R, K and Q are symmetric and one has $C^T = \tilde{C}$. Further, Γ , $\tilde{\Gamma}$, Λ , and $\tilde{\Lambda}$ are third-rank tensors accounting for coupling involving either the shear part of the background flow or the stresslet, and M is a fourth-rank tensor representing the coupling between the shear and the stresslet, with similar properties deduced from the symmetry of R.

An important property of the grand resistance tensor is that it is independent of the boundary conditions associated to a given resistance problem. In other words, for a given viscosity μ and once fixed a system of coordinates, the grand resistance tensor \mathbf{R} depends only on the shape of the object, *i.e.* its surface \mathscr{S} . A change of coordinates or an affine transformation applied to \mathscr{S} modifies the entries of \mathbf{R} through standard linear transformations. For that reason, here we fix a reference frame once and for all and carry the shape optimisation within this frame; which means in particular that we distinguish shapes that do not overlap in the reference frame, even if they are in fact identical after an affine transformation.

With these coordinates considerations aside, we can argue that the grand resistance tensor constitutes an intrinsic characteristic of an object; and all the relevant information about the hydrodynamic resistance of a certain shape is carried in the finite number of entries in \mathbf{R} . While these entries can be obtained by direct calculation in the case of simple geometries, in most cases their value must be determined by solving a particular resistance problem and using Equations (2.4)-(2.5). For example, to determine K_{ij} , one can set \mathbf{U} as unit translation along \mathbf{e}_j , $\mathbf{U} = \mathbf{e}_j$. Then Equation (2.6), combined with (2.4), gives

$$K_{ij} = \mathbf{F}^h \cdot \mathbf{e}_i = -\int_{\mathscr{L}} (\boldsymbol{\sigma}[\mathbf{u}, p] \mathbf{n}) \cdot \mathbf{e}_i d\mathscr{S}.$$

The same strategy can be applied for other entries of R, setting appropriate boundary conditions U and U^{∞} in the Stokes equation and calculating the appropriate projection of F^h or T^h along one of the basis vectors. Figure 1 displays a few illustrative examples. In fact, let us define the generic quantity J_V as the surface integral

$$J_{\mathbf{V}}(\mathscr{S}) = -\int_{\mathscr{S}} (\boldsymbol{\sigma}[\boldsymbol{u}, p]\boldsymbol{n}) \cdot \mathbf{V} d\mathscr{S}. \tag{2.7}$$

Then, judicious choices of U, U^{∞} and V, summarised in Table 1, allow to obtain any coefficient of the grand resistance tensor from formula (2.7).

Of note, for the determination of the coefficients lying on the diagonal of \mathbf{R} , another relation involving power instead of hydrodynamic force is sometimes found [32]. Indeed, the energy dissipation rate η is defined as $\eta = \int_{\mathcal{V}} 2\mu \mathbf{e}[u] : \mathbf{e}[\mathbf{u}] d\mathbf{V}$. In the case of the translation \mathbf{U} of a rigid body, one also has $\eta = \mathbf{F} \cdot \mathbf{U}$. Then, to determine for instance K_{11} , one sets $\mathbf{U} = \mathbf{e}_1$ as described above and obtains

$$K_{11} = \int_{\mathcal{V}} 2\mu e_{1j} e_{1j} d\mathcal{V}.$$

$J_{m{V}}$	$oldsymbol{U}$	\boldsymbol{V}	$oldsymbol{U}_{\infty}$
K_{ij}	$oldsymbol{e}_j$	$oldsymbol{e}_i$	0
C_{ij}	$oldsymbol{e}_j imes oldsymbol{x}$	$oldsymbol{e}_i$	0
$ ilde{C}_{ij}$	$oldsymbol{e}_j$	$oldsymbol{e}_i imes oldsymbol{x}$	0
Q_{ij}	$oldsymbol{e}_j imes oldsymbol{x}$	$oldsymbol{e}_i imes oldsymbol{x}$	0
Γ_{ijk}	0	$oldsymbol{e}_i$	$x_k \boldsymbol{e}_j$
Λ_{ijk}	0	$oldsymbol{e}_i imes oldsymbol{x}$	$x_k \boldsymbol{e}_j$

TABLE 1. Entries of the grand resistance tensor associated to J with respect to the choice of U, V and U^{∞} .

This last expression yields in particular the important property that the diagonal entries of R are positive. Nonetheless, in the following we will prefer the use of formula (2.7) that conveniently works for both diagonal and extradiagonal entries.

2.3. Towards a shape optimisation framework. Seeing J_V as a functional depending on the surface $\mathscr S$ of the object, we will now seek to optimise the shape $\mathscr S$ with J_V as an objective function; in other terms, we want to optimise one of the parameters accounting for the hydrodynamic resistance of the object. As is usually done in shape optimisation, it is relevant in our framework to add some constraint on the optimisation problem. This is both motivated by our wish to obtain relevant and non-trivial shapes (e.g. a shape occupying the whole computational domain), but also to model manufacturing constraints. In this domain, there are multiple choices. In the following, we will focus on the standard choice: $vol(\mathscr S) = V_0$ for some positive parameter V_0 , where $vol(\mathscr S)$ stands for the volume of the domain enclosed by $\mathscr S$.

The *generic* resulting shape optimisation problem we will tackle in what follows hence reads:

$$\left| \min_{\mathscr{S} \in \mathscr{O}_{ad,V_0}} J_{\mathbf{V}}(\mathscr{S}) \right| \tag{2.8}$$

where \mathcal{O}_{ad,V_0} denotes the set of all connected domains \mathcal{S} included in a bounded domain \mathcal{B} such that $\operatorname{vol}(\mathcal{S}) = V_0$. Of note, when performing optimisation in practice, we will also occasionally consider $\max J_{\mathbf{V}}(\mathcal{S})$ instead of $\min J_{\mathbf{V}}(\mathcal{S})$ in (2.8), which is immaterial to the following analysis as it amounts to replacing $J_{\mathbf{V}}(\mathcal{S})$ by $-J_{\mathbf{V}}(\mathcal{S})$.

In this work, we do not address the complete theoretical framework of existence or regularity for minimizers of (2.8). More generally, very few results are available on such questions for models arising from fluid mechanics, and even more broadly for vector-valued problems.

For general results and techniques on existence and regularity in shape optimisation problems, we refer for instance to [20, 22, 25, 51]. We also refer to [24], which establishes a general existence result among quasi-open sets for an extremal spectral problem in fluid mechanics. We remark that the choice of admissible set and regularity assumptions has a decisive impact on existence and on the behaviour of numerical algorithms: an overly permissive admissible class may preclude the existence of a minimizer or lead to singular limit shapes (for example cusps or self-intersections). For clarity, the numerical examples below are computed under the implicit assumption of sufficiently regular boundaries; detailed analytical questions about existence under weaker assumptions are left for future work.

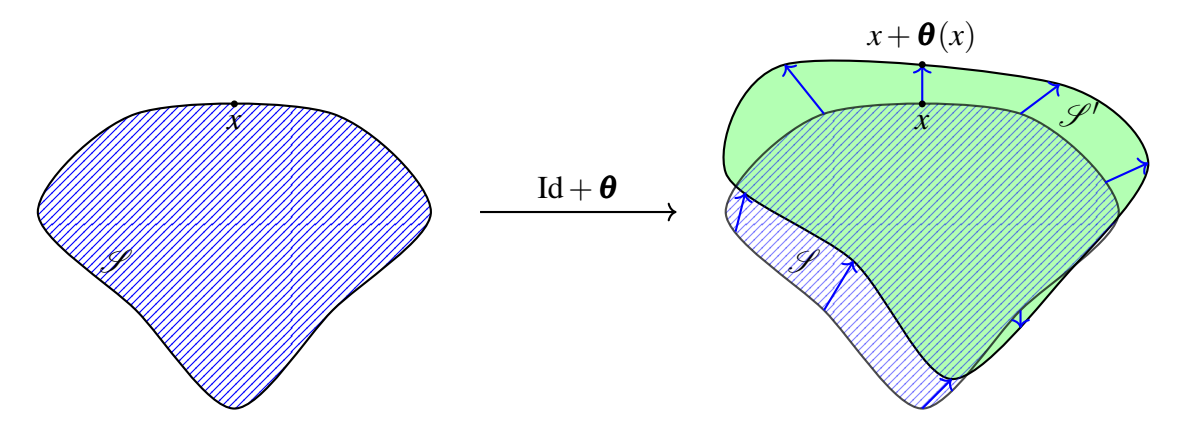


FIGURE 2. Shape optimisation principle: the surface $\mathscr S$ of the body is deformed with respect to a certain vector field $\boldsymbol{\theta} \in \Theta_{\rm ad}$, such that the deformed shape $\mathscr S_{\boldsymbol{\theta}} = (\operatorname{Id} + \boldsymbol{\theta})(\mathscr S)$ improves the objective, *i.e.* satisfies $J(\mathscr S_{\boldsymbol{\theta}}) < J(\mathscr S)$.

3. Analysis of the shape optimisation problem

We recall that the Sobolev space $W^{k,\infty}(\mathbb{R}^3,\mathbb{R}^3)$ is defined as the set of all vector fields $f:\mathbb{R}^3\to\mathbb{R}^3$ such that for every multi-index α with $|\alpha|\leq k$, the mixed partial derivative $D^\alpha f$ exists in a distributional sense and belongs to $L^\infty(\mathbb{R}^3,\mathbb{R}^3)$. It defines a Banach space, equipped with the norm

$$\|f\|_{W^{k,\infty}(\mathbb{R}^3,\mathbb{R}^3)} := \max_{|\alpha| \le k} \|D^{\alpha}f\|_{L^{\infty}(\mathbb{R}^3,\mathbb{R}^3)}.$$

For an open set \mathscr{V} of \mathbb{R}^3 , we let $H^k(\mathscr{V})$ denote the Sobolev space of functions $v \in L^2(\mathscr{V})$ such that for every multi-index α with $|\alpha| \leq k$, its α -th derivative of the sense of distributions belongs to $L^2(\mathscr{V})$.

3.1. **Shape derivatives and deformation fields.** In this section, we recall the notions of domain variation and shape gradient that we will rely on to introduce our main result.

Notion of shape derivative. In this section we introduce the basic tools of shape calculus used throughout the paper. We adopt the Hadamard boundary-variation framework and introduce the *shape derivative*, i.e. the first variation of the objective functional induced by a well chosen infinitesimal deformation of the domain. This object encodes the sensitivity of J to geometric perturbations and, under the usual regularity hypotheses, admits the classical Hadamard boundary integral representation (see below). Precise admissibility and regularity assumptions on deformation fields, as well as remainders on the notion of shape differentiability, will be given in the sequel; for a comprehensive exposition we refer the reader to [2, 26].

In the Hadamard framework, the sensitivity of a shape functional is evaluated by small perturbations of the boundary. For a reference domain $\mathscr{S} \subset \mathbb{R}^3$ we thus consider perturbed domains of the form

$$\mathscr{S}_{\boldsymbol{\theta}} = (\mathrm{Id} + \boldsymbol{\theta})(\mathscr{S}),$$

where $\boldsymbol{\theta}: \mathbb{R}^3 \to \mathbb{R}^3$ is a deformation field that is "small" in a suitable norm. Precise admissibility and regularity hypotheses on $\boldsymbol{\theta}$, as well as the rigorous definition of shape differentiability, are

given below; here it suffices to note that for such small deformations the map $\mathrm{Id} + \boldsymbol{\theta}$ is a \mathscr{C}^2 -diffeomorphism and $\partial \mathscr{S}_{\boldsymbol{\theta}}$ remains a \mathscr{C}^2 hypersurface. The operation $\mathscr{S} \mapsto \mathscr{S}_{\boldsymbol{\theta}}$ is called a *domain variation*.

For practical applications, the main objective is then to construct a suitable vector field $\boldsymbol{\theta}$, chosen in such a way that $\mathscr{S}_{\boldsymbol{\theta}}$ satisfies the constraints of the problem but also that the objective function decreases, ideally strictly, but most methods only guarantee the inequality $J(\mathscr{S}_{\boldsymbol{\theta}}) \leq J(\mathscr{S})$. In the terminology of optimisation, such a deformation vector field is called a descent direction, according to the last inequality. In numerical optimisation, descent methods are expected to bring the shape towards a local optimum for the objective criterion.

Remark 3.1 (Regularity of admissible deformations). For the purposes of this paper we shall restrict attention to domains $\mathscr{V}_0 \subset \mathbb{R}^3$ of class \mathscr{C}^2 . Accordingly, we only consider deformation (velocity) fields $\boldsymbol{\theta} \in W^{3,\infty}(\mathbb{R}^3;\mathbb{R}^3)$. The choice $\boldsymbol{\theta} \in W^{3,\infty}$ is made for convenience and robustness: by Sobolev embedding we have $W^{3,\infty}(\mathscr{V}_0) \hookrightarrow C^{2,1}(\overline{\mathscr{V}_0})$, so each component of $\boldsymbol{\theta}$ is twice continuously differentiable with Lipschitz continuous second derivatives. Standard Cauchy–Lipschitz results for ODEs and flow-regularity porperties then imply that, for $|\varepsilon|$ sufficiently small, $\mathrm{Id} + \varepsilon \boldsymbol{\theta}$ is a \mathscr{C}^2 -diffeomorphism of \mathbb{R}^3 . In particular, it can be shown that, if $\partial \mathscr{V}_0 \in \mathscr{C}^2$, then the deformed boundary $\partial \mathscr{V}_{\varepsilon} := (\mathrm{Id} + \varepsilon \boldsymbol{\theta})(\partial \mathscr{V}_0)$ is a \mathscr{C}^2 hypersurface for small ε , so geometric quantities such as, for instance, the unit normal and the principal curvatures are well defined and vary continuously with ε .

Definition 3.1. Let $\mathscr{S} \in \mathscr{O}_{ad,V_0}$ be a shape and $\boldsymbol{\theta} \in \Theta_{ad}$. We say that the functional J is $(Fr\acute{e}chet)$ shape differentiable at \mathscr{S} if there exists a bounded linear form $W^{3,\infty} \ni \boldsymbol{\theta} \mapsto \langle \mathrm{d}J(\mathscr{S}), \boldsymbol{\theta} \rangle$ such that the following expansion holds:

$$J(\mathscr{S}_{\boldsymbol{\theta}}) = J(\mathscr{S}) + \langle dJ(\mathscr{S}), \boldsymbol{\theta} \rangle + o(\boldsymbol{\theta}), \quad \text{where } \frac{o(\boldsymbol{\theta})}{\|\boldsymbol{\theta}\|_{W^{3,\infty}}} \to 0 \text{ as } \boldsymbol{\theta} \to 0.$$
 (3.1)

In that case, $\langle dJ(\mathcal{S}), \boldsymbol{\theta} \rangle$ is called *shape derivative of* \mathcal{S} *in the direction* $\boldsymbol{\theta}$.

In particular, the *shape derivative of J at \mathcal{S} in the direction* $\boldsymbol{\theta}$ can be computed through the directional derivative

$$\langle \mathrm{d}J(\mathscr{S}), \boldsymbol{\theta} \rangle = \lim_{\varepsilon \searrow 0} \frac{J((\mathrm{Id} + \varepsilon \boldsymbol{\theta})(\mathscr{S})) - J(\mathscr{S})}{\varepsilon}.$$

Deformation vector field. We now make the set of admissible vector fields, $\Theta_{\rm ad}$, explicit. Let \mathcal{V}_0 denote an open bounded subset of \mathbb{R}^3 with a \mathscr{C}^2 boundary and let $\boldsymbol{\theta}$ belong to $W^{3,\infty}(\mathbb{R}^3,\mathbb{R}^3)$ and such that $\|\boldsymbol{\theta}\|_{W^{3,\infty}(\mathbb{R}^3,\mathbb{R}^3)} < 1$. Then $(\mathrm{Id} + \boldsymbol{\theta})(\mathcal{V}_0)$ is an open bounded domain whose boundary is of class \mathscr{C}^2 . Furthermore, $\mathrm{Id} + \boldsymbol{\theta}$ is a diffeomorphism and one has $(\mathrm{Id} + \boldsymbol{\theta})(\partial \mathscr{V}_0) = \partial((\mathrm{Id} + \boldsymbol{\theta})(\mathscr{V}_0))$.

As a consequence, since one aims at dealing with domains having a \mathscr{C}^2 boundary, so that solutions of the involved PDEs will be understood in a strong sense, we will deal with vector fields $\boldsymbol{\theta}$ in

$$\Theta_{ad} = \left\{ \boldsymbol{\theta} \in W^{3,\infty}(\mathbb{R}^3,\mathbb{R}^3), \, \boldsymbol{\theta} = 0 \text{ in } \mathbb{R}^3 \setminus \overline{\mathscr{B}} \text{ and } \|\boldsymbol{\theta}\|_{W^{3,\infty}(\mathbb{R}^3,\mathbb{R}^3)} < 1 \right\}.$$

It is notable that, according to Definition 3.1, shape differentiability of J at \mathcal{V}_0 in direction $\boldsymbol{\theta}$ is equivalent to the standard notion of differentiability at 0 of the domain-variation mapping

$$egin{array}{ccc} \Theta_{\mathrm{ad}} &
ightarrow & \mathbb{R} \\ oldsymbol{ heta} & oldsymbol{ heta} & J(\mathscr{S}_{oldsymbol{ heta}}). \end{array}$$

Remark 3.2 (Practical use of shape derivatives). From a computational and numerical point of view, the expression of the shape derivative in Equation (3.1) suggests that the deformation Θ_{ad} should be chosen such that $\langle dJ(\mathcal{S}), \boldsymbol{\theta} \rangle$ is negative, effectively decreasing the objective criterion at first order. A classical strategy to achieve this goal (see [2, Chapter 6]) consists in deriving an explicit and workable expression of the shape derivative as a surface integral of the form

$$\langle \mathrm{d}J(\mathscr{S}), \boldsymbol{\theta} \rangle = \int_{\mathscr{S}} G(\boldsymbol{x}) \boldsymbol{\theta} \cdot \boldsymbol{n} \mathrm{d}\mathscr{S}(\boldsymbol{x}), \tag{3.2}$$

where G is a function called *shape gradient* of the involved functional. Such a rewriting is in general possible for generic cost functions (according to the structure theorem, see, e.g., [26, Section 5.9]), but usually requires some work, and involves the determination of the adjoint of a linear operator. Once an expression of type (3.2) has been obtained, it is then easy to prescribe the descent direction such that the shape derivative is negative, by choosing for instance $\theta(x) = -G(x)n$, or less straightforward expressions yielding suitable numerical properties; see section 4.1 for further discussion.

3.2. Shape derivative formula for problem (2.8). Before characterizing the shape derivative of the problem under consideration, we first clarify in what sense the solution of System (2.3) is defined and what regularity it possesses.

We refer to [19, Chapter 4], and in particular the theorems IV.1.1 and IV.5.1.

Proposition 3.1. Let us assume that $\mathscr S$ is of class $\mathscr C^2$. Under the compatibility conditions

$$\int_{\mathscr{L}} \boldsymbol{U} \cdot \boldsymbol{n} d\mathscr{L} + \int_{\Gamma} \boldsymbol{U}^{\infty} \cdot \boldsymbol{n} d\Gamma = 0, \tag{3.3}$$

where $\Gamma = \partial \mathcal{B}$, System (2.3) has a unique solution (\mathbf{u}, p) belonging moreover to $[H^2(\mathcal{V})]^3 \times H^1(\mathcal{V})$.

Finally, it can be observed that (3.3) is automatically satisfied for the boundary data (U, U^{∞}) defined by (2.2) and (2.1). Indeed, by using the divergence theorem, one has

$$\int_{\Gamma} \boldsymbol{U}^{\infty} \cdot \boldsymbol{n} d\Gamma = \int_{\mathcal{B}} \nabla \cdot \boldsymbol{U}^{\infty} d\mathscr{V} = 0.$$

Indeed, the divergence of the cross product vanishes obviously. Regarding the term $\nabla \cdot (\boldsymbol{E}^{\infty}\boldsymbol{x})$, we conclude by using that the trace of \boldsymbol{E}^{∞} is equal to zero, since \boldsymbol{E}^{∞} is the shear flow component of \boldsymbol{U}^{∞} .

The term $\int_{\mathscr{L}} \mathbf{U} \cdot \mathbf{n} d\mathscr{S}$ can be handled similarly.

In order to state our main result, let us introduce the pair (\mathbf{v}, q) called *adjoint states* for the optimisation problems we will deal with, as the unique solution of the Stokes problem

$$\begin{cases}
\mu \Delta \mathbf{v} - \nabla q = \mathbf{0} & \text{in } \mathcal{V}, \\
\nabla \cdot \mathbf{v} = 0 & \text{in } \mathcal{V}, \\
\mathbf{v} = \mathbf{V} & \text{on } \mathcal{S}, \\
\mathbf{v} = \mathbf{0} & \text{on } \partial \mathcal{B}.
\end{cases} (3.4)$$

Then, one can express the shape derivative and shape gradient with respect to the solution of resistance problem (2.3) and adjoint problem (3.4):

Theorem 3.1. Let $\mathscr{S} \in \mathscr{O}_{ad,V_0}$ and $\boldsymbol{\theta} \in \Theta_{ad}$. The functional $J_{\boldsymbol{V}}$ is shape differentiable. Furthermore, for all $\boldsymbol{\theta} \in \Theta_{ad}$, one has

$$\langle dJ_{\mathbf{V}}(\mathscr{S}), \mathbf{\theta} \rangle = 2\mu \int_{\mathscr{S}} (\mathbf{e}[\mathbf{u}] : \mathbf{e}[\mathbf{v}] - \mathbf{e}[\mathbf{U}] : \mathbf{e}[\mathbf{v}] - \mathbf{e}[\mathbf{u}] : \mathbf{e}[\mathbf{V}]) (\mathbf{\theta} \cdot \mathbf{n}) d\mathscr{S}, \tag{3.5}$$

and the shape gradient G is therefore given by

$$G = 2\mu \left(\mathbf{e}[\mathbf{u}] : \mathbf{e}[\mathbf{v}] - \mathbf{e}[\mathbf{U}] : \mathbf{e}[\mathbf{v}] - \mathbf{e}[\mathbf{u}] : \mathbf{e}[\mathbf{V}] \right).$$

Remark 3.3. If we assume moreover that U and V satisfy e[U] = e[V] = 0 in \mathcal{V} , which is trivially true for all the relevant choices of U and V displayed in Table 1 – and more generally for any linear flow and rigid body motion – then the shape gradient simply becomes $G = 2\mu e[u]$: e[v], which is the expression we will use later on when implementing the shape optimisation algorithm.

Proof of Theorem 3.1. To compute the shape gradient of the functional J_V , which is expressed as a surface integral, a standard technique (see [26, Chapter 5]) first consists in rewriting it under volumetric form.

We will make use of the following integration-by-parts identity, well-known in the framework of fluid mechanics and straightforward to prove by direct calculation:

Lemma 3.1. Let **u** and **v** denote two vector fields in $H^2(\mathcal{V})$. Then,

$$2\int_{\mathcal{V}} \boldsymbol{e}[\boldsymbol{u}] : \boldsymbol{e}[\boldsymbol{v}] d\mathcal{V} = -\int_{\mathcal{V}} (\Delta \boldsymbol{v} + \nabla(\nabla \cdot \boldsymbol{v})) \cdot \boldsymbol{u} d\mathcal{V} + 2\int_{\partial \mathcal{V}} \boldsymbol{e}[\boldsymbol{v}] \boldsymbol{n} \cdot \boldsymbol{u} d\mathcal{S}. \tag{3.6}$$

Let us multiply the main equation of (2.3) by ν . Applying identity (3.6), one sees that

$$2\mu \int_{\mathcal{Y}} \boldsymbol{e}[\boldsymbol{u}] : \boldsymbol{e}[\boldsymbol{v}] d\mathcal{V} - \int_{\mathcal{Y}} p \nabla \cdot \boldsymbol{v} d\mathcal{V} - 2 \int_{\partial \mathcal{Y}} \boldsymbol{\sigma}[\boldsymbol{u}, p] \boldsymbol{n} \cdot \boldsymbol{v} d\mathcal{S} = 0.$$

By plugging the boundary conditions into this equality, one has $-J_{\mathbf{V}}(\mathscr{S}) = 2\mu \int_{\mathscr{V}} \mathbf{e}[\mathbf{u}] : \mathbf{e}[\mathbf{v}] d\mathscr{V}$. We are now ready to differentiate this relation with respect to the variations of the domain \mathscr{S} . To this end, we will use the formula for the derivative of integrals on a variable domain, shown in [26, Theorem 5.2.2].

$$-\langle dJ_{\mathbf{V}}(\mathscr{S}), \mathbf{\theta} \rangle = 2\mu \int_{\mathscr{S}} \mathbf{e}[\mathbf{u}] : \mathbf{e}[\mathbf{v}](\mathbf{\theta} \cdot \mathbf{n}) d\mathscr{S} + 2\mu \int_{\mathscr{V}} \mathbf{e}[\mathbf{u}'] : \mathbf{e}[\mathbf{v}] d\mathscr{V} + 2\mu \int_{\mathscr{V}} \mathbf{e}[\mathbf{u}] : \mathbf{e}[\mathbf{v}'] d\mathscr{V},$$
(3.7)

where $(\boldsymbol{u'},p')$ and $(\boldsymbol{v'},q')$ may be interpreted as characterising the hypothetical behaviour of the fluid within \mathscr{B} if the surface \mathscr{S} was moving at a speed corresponding to the deformation $\boldsymbol{\theta} \in \Theta_{ad}$. The quantities $(\boldsymbol{u'},p')$ and $(\boldsymbol{v'},q')$ are thus solutions of the Stokes-like systems

$$\begin{cases} \mu \Delta \boldsymbol{u'} - \nabla p' = \boldsymbol{0} & \text{in } \mathcal{V}, \\ \nabla \cdot \boldsymbol{u'} = 0 & \text{in } \mathcal{V}, \\ \boldsymbol{u'} = -[\nabla (\boldsymbol{u} - \boldsymbol{U})] \boldsymbol{n} (\boldsymbol{\theta} \cdot \boldsymbol{n}) & \text{on } \mathcal{S}, \\ \boldsymbol{u'} = \boldsymbol{0} & \text{on } \partial \mathcal{B}, \end{cases}$$

and

$$\begin{cases} \mu \Delta \mathbf{v'} - \nabla q' = \mathbf{0} & \text{in } \mathcal{V}, \\ \nabla \cdot \mathbf{v'} = 0 & \text{in } \mathcal{V}, \\ \mathbf{v'} = -[\nabla (\mathbf{v} - \mathbf{V})] \mathbf{n} (\mathbf{\theta} \cdot \mathbf{n}) & \text{on } \mathcal{S}, \\ \mathbf{v'} = \mathbf{0} & \text{on } \partial \mathcal{B}. \end{cases}$$

Let us rewrite the two last terms of the sum in (3.7) under a convenient form for algorithmic issues. From Eq. (3.6), one gets

$$2\mu \int_{\mathcal{V}} \boldsymbol{e}[\boldsymbol{u'}] : \boldsymbol{e}[\boldsymbol{v}] d\mathcal{V} = \mu \int_{\mathcal{V}} (-\Delta \boldsymbol{v} + \nabla(\nabla \cdot \boldsymbol{v})) \cdot \boldsymbol{u'} d\mathcal{V} + 2\mu \int_{\mathcal{S}} \boldsymbol{e}[\boldsymbol{v}] \boldsymbol{n} \cdot \boldsymbol{u'} d\mathcal{S}.$$

Using the relations contained in Eqs. (3.4) for v and (3.2) for u' yields

$$2\mu \int_{\mathcal{V}} \boldsymbol{e}[\boldsymbol{u'}] : \boldsymbol{e}[\boldsymbol{v}] d\mathcal{V} = -\int_{\mathcal{V}} \nabla q \cdot \boldsymbol{u'} d\mathcal{V} - 2\mu \int_{\mathcal{S}} (\boldsymbol{\theta} \cdot \boldsymbol{n}) \boldsymbol{e}[\boldsymbol{v}] \boldsymbol{n} \cdot \nabla (\boldsymbol{u} - \boldsymbol{U}) \boldsymbol{n} d\mathcal{S},$$
$$= -\int_{\mathcal{S}} q \boldsymbol{u'} \cdot \boldsymbol{n} d\mathcal{S} - 2\mu \int_{\mathcal{S}} (\boldsymbol{\theta} \cdot \boldsymbol{n}) \boldsymbol{e}[\boldsymbol{v}] \boldsymbol{n} \cdot \nabla (\boldsymbol{u} - \boldsymbol{U}) \boldsymbol{n} d\mathcal{S}.$$

Since u - U vanishes on \mathcal{S} and is divergence-free, and defining the derivative with respect to the normal by $\frac{\partial}{\partial n} x_i = \frac{\partial x_i}{\partial x_i} n_j$, one has

$$m{n} \cdot
abla (m{u} - m{U}) m{n} = rac{\partial (u_i - U_i)}{\partial x_j} n_j n_i = rac{\partial (u_i - U_i)}{\partial m{n}} n_i$$

$$= rac{\partial (u_i - U_i)}{\partial x_i} =
abla \cdot (m{u} - m{U}) = 0 \quad \text{on } \mathscr{S}.$$

Since $\mathbf{n} \cdot \mathbf{n} = 1$, then

$$\sigma[\mathbf{v}, q]\mathbf{n} \cdot \nabla(\mathbf{u} - \mathbf{U})\mathbf{n} = 2\mu \mathbf{e}[\mathbf{v}]\mathbf{n} \cdot \nabla(\mathbf{u} - \mathbf{U})\mathbf{n} \quad \text{on } \mathcal{S}. \tag{3.8}$$

which leads to

$$2\mu \int_{\mathcal{Y}} \boldsymbol{e}[\boldsymbol{u'}] : \boldsymbol{e}[\boldsymbol{v}] d\mathcal{Y} = -\int_{\mathcal{S}} (\boldsymbol{\theta} \cdot \boldsymbol{n}) \boldsymbol{\sigma}[\boldsymbol{v}, q] \boldsymbol{n} \cdot \nabla (\boldsymbol{u} - \boldsymbol{U}) \boldsymbol{n} d\mathcal{S}. \tag{3.9}$$

Using straightforward calculations as carried in [11, Lemma 1], we can moreover show that

$$e[v]n \cdot \nabla (u - U)n = e[v] : e[u - U],$$

yielding a more symmetrical expression for (3.8):

$$\sigma[\mathbf{v},q]\mathbf{n}\cdot\nabla(\mathbf{u}-\mathbf{U})\mathbf{n}=2\mu\mathbf{e}[\mathbf{v}]\mathbf{n}\cdot\mathbf{e}[\mathbf{u}-\mathbf{U}]\mathbf{n}$$
 on \mathscr{S} .

It follows that (3.9) can be rewritten as

$$2\mu \int_{\mathcal{Y}} \mathbf{e}[\mathbf{u'}] : \mathbf{e}[\mathbf{v}] d\mathcal{V} = -2\mu \int_{\mathcal{S}} (\mathbf{\theta} \cdot \mathbf{n}) \mathbf{e}[\mathbf{v}] : \mathbf{e}[\mathbf{u} - \mathbf{U}] d\mathcal{S}. \tag{3.10}$$

By mimicking the computation above, we obtain similarly

$$2\mu \int_{\mathscr{V}} \boldsymbol{e}[\boldsymbol{u}] : \boldsymbol{e}[\boldsymbol{v'}] d\mathscr{V} = -2\mu \int_{\mathscr{S}} (\boldsymbol{\theta} \cdot \boldsymbol{n}) \boldsymbol{e}[\boldsymbol{u}] : \boldsymbol{e}[\boldsymbol{v} - \boldsymbol{V}] d\mathscr{S}. \tag{3.11}$$

Gathering (3.7), (3.10) and (3.11) yields

$$-\langle dJ_{\mathbf{V}}(\mathscr{S}), \mathbf{\theta} \rangle = 2\mu \int_{\mathscr{S}} (\mathbf{\theta} \cdot \mathbf{n}) \left(\mathbf{e}[\mathbf{u}] : \mathbf{e}[\mathbf{v}] - \mathbf{e}[\mathbf{v}] : \mathbf{e}[\mathbf{u} - \mathbf{U}] - \mathbf{e}[\mathbf{u}] : \mathbf{e}[\mathbf{v} - \mathbf{V}] \right) d\mathscr{S},$$

and rearranging the terms finally leads to the expected expression of the shape derivative (3.1) and concludes the proof of Proposition 3.1.

The shape gradient yields a natural first-order descent criterion: if J is shape-differentiable at $\mathscr S$ and a deformation field $\boldsymbol \theta$ satisfies $\langle \mathrm{d} J(\mathscr S), \boldsymbol \theta \rangle < 0$, then by the expansion (3.1), there exists $\varepsilon_0 > 0$ such that $J(\mathscr S_{\varepsilon \boldsymbol \theta}) < J(\mathscr S)$ for every $0 < \varepsilon < \varepsilon_0$. Thus a negative shape derivative guarantees infinitesimal decrease; the statement is inherently local, and its validity depends on the smallness of the perturbation in the chosen norm (for instance $\|\cdot\|_{W^{3,\infty}}$ or a suitable Sobolev norm).

In practice, however, naively using the pointwise shape gradient or taking overly large steps quickly undermines this linearised guarantee. Directions with large high-frequency or tangential components deliver only marginal first-order gains while amplifying higher-order remainders, which produces spurious boundary oscillations, loss of \mathcal{C}^2 regularity and mesh deterioration. Likewise, finite deformations may activate nonlinear effects and violate geometric constraints (volume, admissible topology or regularity), so that a finite-step update can increase the objective or leave the admissible class even when the infinitesimal criterion is satisfied.

To obtain stable, convergent algorithms one therefore must control both the direction and the magnitude of updates. It is common to replace the raw boundary gradient by a smoothed (Sobolev or H^1) gradient to suppress high frequencies and enforce regularity of $\boldsymbol{\theta}$ and to consider a step-size rule (e.g., line search) so that the linear term dominates the remainder.

Overall, we have shown in this section that the shape derivative for the optimisation of any entry of the grand resistance tensor comes down to a single formula (3.5), which depends on the solutions to two appropriately chosen resistance problems. In the next section, we develop a numerical algorithm to apply this result to the computation of various optimised shapes.

4. Numerical Implementation

4.1. **Descent direction.** In this section, we focus on how to prescribe the descent direction $\boldsymbol{\theta}$ from (3.5). As evoked in the previous section, the most natural idea consists in choosing $\boldsymbol{\theta} = -G\boldsymbol{n}$, ensuring that a small domain variation in this direction decreases the objective function. However, this simple choice can yield vector fields that are not smooth enough, typically leading to numerical instability (see [14]). To address this issue, a classical method consists in using a variational formulation involving the derivative of $\boldsymbol{\theta}$. More precisely, we want to find a field $\boldsymbol{\theta}$ that satisfies the following identity for all $\boldsymbol{\psi} \in H^1(\mathbb{R}^3)$ such that $\boldsymbol{\psi} = 0$ in $\mathbb{R}^3 \setminus \overline{\mathcal{B}}$:

$$\int_{\mathcal{V}} \nabla \boldsymbol{\theta} : \nabla \boldsymbol{\psi} \, d\mathcal{V} = -\langle dJ(\mathcal{S}), \boldsymbol{\psi} \rangle. \tag{4.1}$$

In particular, evaluating this identity at $\boldsymbol{\theta}$ yields $\langle dJ(\mathcal{S}), \boldsymbol{\theta} \rangle = -\int_{\mathcal{V}} |\nabla \boldsymbol{\theta}|^2 d\mathcal{V} \leq 0$, guaranteeing decrease of $J_{\boldsymbol{V}}$. Thus, the variational formulation of Equation (4.1) implicitly defines a 'good' descent direction. To determine the strong formulation of the PDE solved by $\boldsymbol{\theta}$, let us now apply Green's formula on Equation (4.1):

$$-\int_{\mathcal{Y}} \boldsymbol{\psi} \cdot \Delta \boldsymbol{\theta} d\mathcal{Y} + \int_{\mathcal{S}} \boldsymbol{\psi} \cdot (\nabla \boldsymbol{\theta} \boldsymbol{n}) d\mathcal{S} = -\int_{\mathcal{S}} \boldsymbol{\psi} \cdot G \boldsymbol{n} d\mathcal{S}. \tag{4.2}$$

This identity being valid for all ψ , we straightforwardly deduce that θ is solution of the Laplace equation

$$\begin{cases}
-\Delta \boldsymbol{\theta} = \mathbf{0} & \text{in } \mathcal{V}, \\
\boldsymbol{\theta} = \mathbf{0} & \text{on } \partial \mathcal{B}, \\
(\nabla \boldsymbol{\theta}) \cdot \boldsymbol{n} = -G \boldsymbol{n} & \text{on } \mathcal{S}.
\end{cases}$$
(4.3)

Note that the dependence of this problem in the criterion J_V and shape derivative is contained within the boundary condition on \mathcal{S} , in which the shape gradient G appears.

It should be noted that, although the variational formulation provides a rigorously defined descent direction, its practical implementation is more computationally demanding: at each iteration one must solve the PDE system (4.3) to obtain the deformation field $\boldsymbol{\theta}$. Consequently, the cost per iteration is significantly higher than that of simpler heuristic or explicit descent strategies, but the resulting direction is guaranteed to decrease the objective at first order and to preserve the regularity of the domain.

4.2. **Manufacturing constraints.** One typically needs to include so-called *manufacturing* constraints on the shape to prevent it from reaching trivial (shrunk to a single point or expanded to fill the entire fluid domain) or unsuitable (e.g. too thin or too irregular) solutions. As mentioned at the beginning of section 3.1, in this paper, we chose to focus on the standard constraint of a constant volume $vol(\mathcal{S})$ enclosed by the surface \mathcal{S} . Hence, denoting by V_0 the volume of the initial solid, we are considering the *constrained* optimisation problem

$$\max_{\text{vol}(\mathscr{S})=V_0} J_{\mathbf{V}}(\mathscr{S}). \tag{4.4}$$

The volume constraint may be enforced with a range of classical optimisation techniques, among which we will use a so-called "augmented Lagrangian", adapted from [12, Section 3.7] and briefly described in this section. The augmented Lagrangian algorithm converts the constrained optimisation problem (4.4) into a sequence of unconstrained problems (hereafter indexed by n). Hence, we will be led to solve:

$$\inf_{\mathscr{S}}\mathscr{L}(\mathscr{S},\ell^n,b^n),$$

where

$$\mathscr{L}(\mathscr{S},\ell,b) = J(\mathscr{S}) - \ell(\operatorname{vol}(\mathscr{S}) - V_0) + \frac{b}{2}(\operatorname{vol}(\mathscr{S}) - V_0)^2.$$

In this definition, the parameter b is a (positive) penalisation factor preventing the equality constraint 'vol(\mathscr{S}) = V_0 ' to be violated. The parameter ℓ is a Lagrange multiplier associated with this constraint.

The principle of the augmented Lagrangian algorithm rests upon the search for a (local) minimiser S^n of $S \mapsto \mathcal{L}(S, \ell^n, b^n)$ for fixed values of ℓ^n and b^n . Given $\alpha > 1$, these parameters are updated according to the rule:

$$\ell^{n+1} = \ell^n - b^n(\operatorname{vol}(\mathscr{S}^n) - V_0), \text{ and } b^{n+1} = \begin{cases} \alpha b^n & \text{if } b < b_{\text{target}}, \\ b^n & \text{otherwise;} \end{cases}$$
(4.5)

in other terms, the penalisation parameter b is increased during the first iterations until the value b_{target} is reached. This regular increase of b ensures that the domain satisfies the constraint more and more precisely during the optimisation process.

4.3. **Numerical resolution of the PDEs.** For the sake of clarity and replicability of the algorithm described below, we provide some additional information about the numerical resolution of the Stokes and Laplace equations (2.3)-(4.3) required at each step of the deformation.

The surface $\mathscr S$ is first equipped with a triangular surface mesh $\mathscr T$ containing the coordinates of the nodes, the middle of the edges, the center of the elements, and connectivity matrices.

The numerical resolution is then carried out by boundary element method [41] using the BEMLIB Fortran library [43], which allows to determine the force distribution at each point x of the (discretised) surface \mathcal{S} by making use of the integral representation

$$\boldsymbol{u}(\boldsymbol{x}) = \int_{\mathscr{L}} \boldsymbol{G}(\boldsymbol{x} - \boldsymbol{x}_0) \boldsymbol{f}(\boldsymbol{x}_0) d\boldsymbol{x}_0,$$

where \boldsymbol{G} is the Oseen tensor given by

$$G_{ij}(\mathbf{x}) = \frac{1}{\|\mathbf{x}\|} \delta_{ij} + \frac{1}{\|\mathbf{x}\|^3} x_i x_j,$$

with δ_{ij} being the Kronecker delta notation.

Once the force distribution f is known, the rate-of-strain tensors e needed to compute the shape gradient established in formula (3.2) can be conveniently computed through the integral expression

$$e_{ij}(\mathbf{x}) = \int_{\mathscr{S}} \left(\frac{1}{\|\mathbf{x} - \mathbf{x}_0\|^3} \delta_{ij}(\mathbf{x} - \mathbf{x}_0)_k - \frac{3}{\|\mathbf{x} - \mathbf{x}_0\|^5} (\mathbf{x} - \mathbf{x}_0)_i (\mathbf{x} - \mathbf{x}_0)_j (\mathbf{x} - \mathbf{x}_0)_k \right) f_k(\mathbf{x}_0) d\mathscr{S}.$$

4.4. **Shape optimisation algorithm.** We now summarise the main steps of the algorithm.

(1) **Initialisation.**

- Equip the initial shape \mathscr{S}^0 with a mesh \mathscr{T}^0 , as described above.
- Select initial values for the coefficients ℓ^0 , $b^0 > 0$ of the augmented Lagrangian algorithm.

(2) **Main loop: for** $n = 0, \dots$

- (a) Compute the solution (\boldsymbol{u}^n, p^n) to the Stokes system (2.3) on the mesh \mathcal{T}^n of \mathcal{S}^n ;
- (b) Compute the solution (\mathbf{v}^n, q^n) to the adjoint system (3.4) on the mesh \mathcal{T}^n of \mathcal{S}^n .
- (c) Compute the $L^2(\mathcal{S}^n)$ shape gradient G^n of J, as well as the shape gradient ϕ^n of $\mathcal{S} \mapsto \mathcal{L}(\mathcal{S}, \ell^n, b^n)$ given by

$$\phi^n = G^n - \ell^n + b^n(\operatorname{vol}(\mathscr{S}^n) - V_0).$$

(d) Infer a descent direction $\boldsymbol{\theta}^n$ for $\mathscr{S} \mapsto \mathscr{L}(\mathscr{S}, \ell^n, b^n)$ by solving the PDE

$$\begin{cases}
-\Delta \boldsymbol{\theta} = \mathbf{0} & \text{in } \mathcal{V}^n, \\
\boldsymbol{\theta} = \mathbf{0} & \text{on } \partial \mathcal{B}, \\
(\nabla \boldsymbol{\theta}) \boldsymbol{n} = -\phi^n \boldsymbol{n} & \text{on } \mathcal{S}^n.
\end{cases}$$

on the mesh \mathcal{I}^n .

(e) Find a descent step τ^n such that

$$\mathscr{L}((\mathrm{Id} + \tau^n \boldsymbol{\theta}^n)(\mathscr{S}^n), \ell^n, b^n) < \mathscr{L}(\mathscr{S}^n, \ell^n, b^n).$$

(f) Move the vertices of \mathcal{I}^n according to τ^n and $\boldsymbol{\theta}^n$:

$$\boldsymbol{x}_p^{n+1} = \boldsymbol{x}_p^n + \tau^n \boldsymbol{\theta}^n (\boldsymbol{x}_p^n). \tag{4.6}$$

- If the resulting mesh is invalid, go back to step 2e, and use a smaller value for τ^n ,
- Else, the positions (4.6) define the vertices of the new mesh \mathcal{T}^{n+1} .

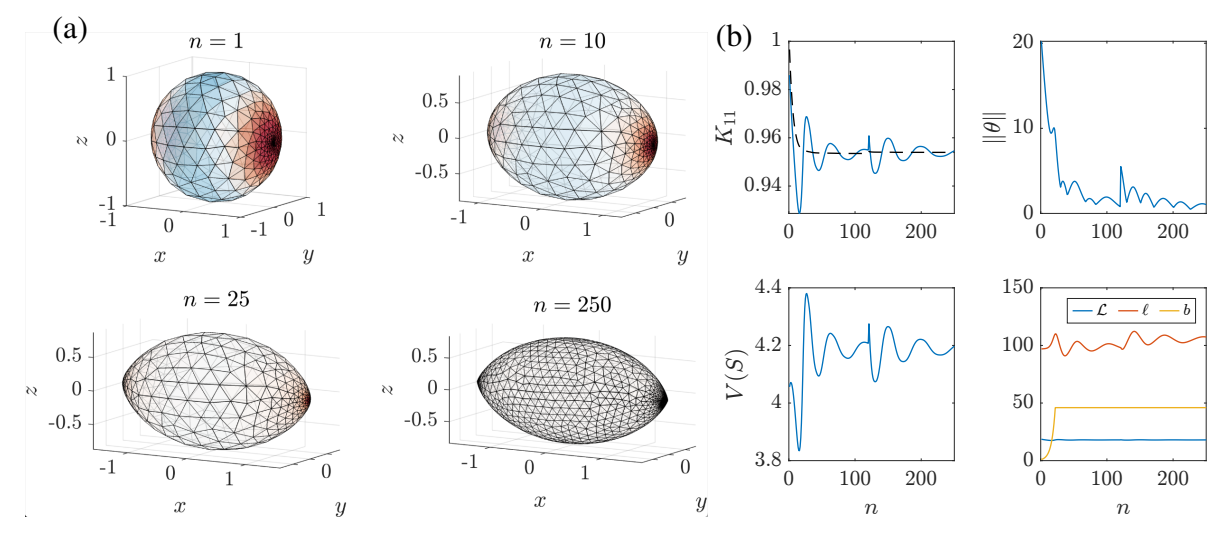


FIGURE 3. Visualisation of the shape optimisation algorithm running through the minimisation of K_{11} . (a) Aspect of the shape at four stages of the alrgorithm. The surface colours on the top row represent the shape gradient value (from red for a high value for outwards deformation to blue for high inwards deformation). Note that the initial mesh is already well-prepared from previous runs and is further refined around iteration 100. (b) Evolution of the values of various parameters along the optimization process.

- (g) If the quality of \mathcal{I}^{n+1} is too low, use a local remeshing.
- (h) Update the augmented Lagrangian parameters according to (4.5).

(3) **Ending criterion.** Stop if

$$\|\boldsymbol{\theta}^n\|_{L^2(S^n)} < \varepsilon_{\text{stop}} \text{ or } n > n_{\text{max}}.$$
 (4.7)

Return \mathcal{S}^n .

5. Numerical Results

In this section, we present various applications of the algorithm with different entries of the resistance tensor as objective functions.

To assess algorithmic robustness, we performed targeted sensitivity studies. These include: (i) a mesh-convergence test showing the objective value and key geometric metrics as the mesh is refined; (ii) multiple runs from different initial shapes (sphere, prolate ellipsoid, and a perturbed sphere) to reveal the presence of local minima; and (iii) a diagnostic of the augmented Lagrangian multipliers and step-size choice to explain stabilization strategies. The algorithm's stopping criteria are made explicit: iteration terminates when either (a) the deformation field satisfies $|\boldsymbol{\theta}|_{L^2(\partial\Omega)} < \varepsilon$, (b) a prescribed maximum number of iterations is reached, (c) a maximum number of boundary elements is reached after remeshing (meaning the surface has become increasingly complex with locally high curvature values), or (d) a geometric intersection (self-overlap) is detected by the collision test. Where a run ends because of criteria (b), (c) or (d), the resulting shape should be interpreted as a numerical limit of the deformation procedure rather than a rigorously computed minimizer.

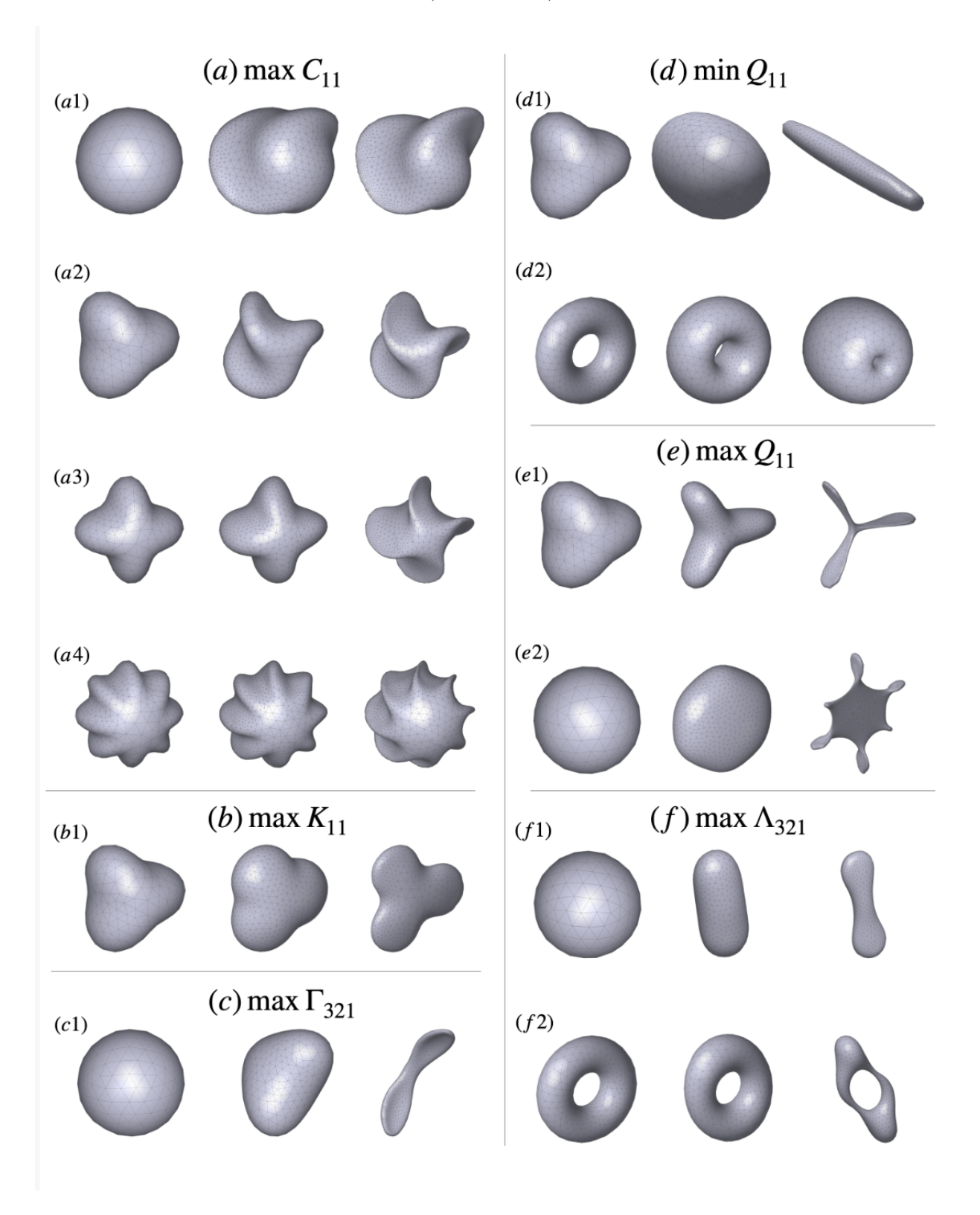


FIGURE 4. Optimised shapes obtained for various objective functions and from different initial shapes. Each series shows, from left to right, the initial shape, an intermediate iteration and the final shape at algorithm termination. Scale may vary from one shape to another.

5.1. **Diagonal parameters.** First, we consider the classical "minimal drag" problem at constant volume, equivalent to the minimisation of K_{11} . The solution to this problem was determined to be an axisymmetric "rugby-ball"-like shape in [42], and has been found again with different methods as well as used as an exemplar in the literature later on.

Applying the shape optimization algorithm described in the previous section, we are able to recover this well-known solution, as shown on Figure 3. Starting from a sphere, the shape gradient G and deformation field θ are represented on the top left plot (a), with the red and blue colours being respectively associated to positive and negative gradient, meaning inward and outward associated deformation. As expected, the deformation vector field tends to stretch the sphere in the x direction in order to decrease its drag. After 10 iterations, the object has taken the shape of an ellipsoid. Of note, axisymmetry, known as a feature of the optimal shape for this problem, is remarkably well preserved along the numerical resolution. At 250 iterations, the ending criterion (4.7) is reached and the algorithm stops, with the resulting shape closely resembling the known optimal solution [42]. The computed value of the final drag coefficient is equal to 0.9540, in excellent agreement with the value known to be the one associated to optimal drag (approx. 0.9542). The small difference is attributable to the relatively coarse meshing and the oscillations of the volume, which decrease overall precision.

The plots on Figure 3b show the evolution of the criterion $J_{V}(\mathcal{S}) = K_{11}$, the L²-norm of the deformation vector field $\|\boldsymbol{\theta}\|$, the volume $\operatorname{vol}(\mathcal{S})$ enclosed by \mathcal{S} along the simulation, and the augmented Lagrangian parameters, with a clear numerical convergence being observed. Of note, the value of K_{11} is directly correlated to the volume $\operatorname{vol}(\mathcal{S})$ of the body, making this particular problem extremely sensitive to volume variations. For that reason, the augmented Lagrangian algorithm with adaptive step described in the previous section was observed to induce instability and amplifying volume oscillations, even with fine tuning of the parameters ℓ and b. In case of K_{11} , the algorithm was adapted to make it more robust by empirically setting a fixed deformation step τ and Lagrange multiplier ℓ to obtain stability and convergence. The parameter values used in figure 3 are $\tau = 10^{-3}$, $\ell = 98.8$, $b_0 = 1$, $b_{\text{target}} = 50$ and $\alpha = 1.03$.

More generally, an adapted choice of augmented Lagrangian parameters is critical to observe convergence of the algorithm, and is highly dependent on the nature of the problem, therefore requiring *ad hoc* tuning for each different objective function.

Now, let us turn to other entries of R. Figure 4 gathers the results for six different objective functions and various initial shapes. We do not aim for an exhaustive list of initial shapes or optima, but rather point out a number of interesting observations when applying the optimisation method described above. We first focus on diagonal entries, namely K_{11} and Q_{11} .

Maximising the translational drag through K_{11} has the effect of flattening the initial shape along the plane perpendicular to the translation direction (Figure 4b1). Shapes minimising Q_{11} can be seen on panel 4d. Rotational drag for the initial objects is reduced by turning it into a body of revolution – note the "quick" disappearance of the 3-fold symmetry in (d1) – and stretching the shape along the rotation axis, until the highest possible slenderness allowed before reaching one of the stopping criteria.

These results suggest that $\max K_{11}$ and $\min Q_{11}$ are achieved respectively by infinitely flat and infinitely slender shapes, meaning that the volume constraint alone is not yielding physically satisfying optima. Additional constraints, for instance on the shape diameter, are warranted for

further investigation. Note that similar issues arise for extradiagonal parameters like K_{12} and Q_{12} (not shown on the figure).

On the other hand, maximising Q_{11} sharpens the 3-fold symmetry of the initial object in Figure 4e1, creating flat wings offering high rotational resistance. When starting from a sphere (Figure 4e2), wings emerge as well, with number and size depending on the initial meshing. This suggests the existence of several local minima and a high sensitivity to initial conditions.

5.2. Extradiagonal parameters. Unlike the diagonal entries K_{ii} and Q_{ii} of the resistance tensor, the extradiagonal entries of the grand resistance tensor are not necessarily positive. In fact, a mirror symmetry in along an appropriately chosen plane will reverse the sign of extradiagonal entries. This observation induces that objects possessing certain planar symmetries have null entries in their resistance tensor; in particular, all the extradiagonal entries of a sphere's resistance tensor are equal to zero. These properties importantly imply that the minimisation and maximisation problems are equivalent when choosing an extradiagonal entry as an objective: one can switch between both by means of an appropriate planar symmetry.

We turn to the optimisation of C_{11} , presented on figure 4a. This parameter accounts for the coupling between torque and translation; hence optimising it means that we are looking for the shape that converts best a rotational effect into directional velocity. Helicoidal shapes are well-known to be capable to achieve this conversion. More generally, C_{11} is nonzero only if the shape possesses some level of chirality. Chirality as measured by C_{11} is widespread among microswimmers, in particular as a possible mean of producing robust directional locomotion within background flows [55].

Optimisation of C_{11} was tackled for a particular class of shapes in [33], in the context of magnetic helicoidal swimmers. Considering slender shapes parametrised by a one-dimensional curve, they find that optimal shapes are given by regular helicoidal folding, with additional considerations on its pitch and radius depending on parameters and on the presence of a head.

Starting from a sphere, we see Figure 4a1 the emergence of two helicoidal wings, that tend to sharpen along the simulation. Other initial shapes with 3-fold, 4-fold and 6-fold symmetry (Figure 4a2,4a3,4a4) similarly become chiral along the optimisation, while keeping their initial symmetry properties. This suggests again the existence of many local optima for this problem, although the stopping criterion in each case occurred because of reaching maximal mesh refinement. Finer handling of the narrow parts of the helix wings may allow to carry on the shape optimisation process and we can conjecture further folding of the shapes into long screw-like shapes.

Finally, we present results, perhaps less intuitive, related to shear-force and shear-torque coupling, namely Γ_{321} and Λ_{321} , on Figure 4c and 4f. For shear-force coupling, a two-wing shape emerges from an initial sphere, with 2-fold rotational symmetry along an axis perpendicular to the shear plane. The wings point to the same direction relative to the shear plane, offering high resistance to the flow in the perpendicular direction. Similar interpretation can be carried for shear-torque coupling, regardless of initial shapes considered (f1,f2).

6. DISCUSSION AND PERSPECTIVES

In this paper, we have addressed the problem of optimal shapes for the resistance problem in a Stokes flow. Considering the entries of the grand resistance tensor as objective shape functionals to optimise, and using the framework of Hadamard boundary variation, we derived a general

formula for the shape gradient, allowing to define the best deformation to apply to any given shape. While this shape optimisation framework is mathematically standard, its usage in the context of microhydrodynamics is limited, mostly circumscribed to the work of [33], and the theoretical results and numerical scheme that we presented here provide a much higher level of generality, both concerning the admissible shapes and the range of objective functions.

After validating the numerical capabilities of the shape optimisation algorithm by comparing the optimal shape for K_{11} to the celebrated result of [42], we investigated the shapes minimising and maximising entries of the resistance tensor. The numerical results reveal new insights on optimal hydrodynamic resistance. In particular, we obtained an optimal profile for the torque drag (Q_{11}) , observed the emergence of chiral, helicoidal structure maximising the force/rotation coupling (C_{11}) , and other intriguing shapes generated when minimising extradiagonal entries. In the context of low-Reynolds number hydrodynamics, these preliminary results may help understand and refine some of the the criteria that are believed to govern the morphology of microscopic bodies [53, 58].

With most of the optimisation problems considered here being highly unconstrained and nonconvex, we can assume that many local extrema exist, and that a range of different results is likely to be observed for different initial shapes. As discussed above, finer handling of the surface mesh to deal with locally high curvature, sharp edges and cusps, and additional manufacturing constraints to prevent self-overlapping and take other criteria into account, are warranted to pursue this broader exploration. Furthermore, seeing as some of the shapes in figure 4 appear to take a torus-like profile from an initial spherical shape, it might be interesting to allow topological modifications of the shape along the optimisation process, which requires different approaches such as the level set method [2].

Furthermore, the computational structure of the optimisation problem is readily adaptable to more complex objective criteria defined as functions of entries of the grand resistance tensor, which allows to tackle relevant quantities for various applications. A prototypical example would be to seek extremal values for the Bretherton parameter B [8], a geometrical parameter for the renowned Jeffery equations [30] which describe the behaviour of an axisymmetric object in a shear flow. As noted by [29], B can be expressed as a rational function of seven distinct entries of the grand resistance tensor. For spheroids, B lies between -1 and 1, but nothing theoretically forbids it from being greater than 1 or smaller than -1; yet exhibiting realistic shapes achieving it is notoriously difficult [8, 48]. Further, another geometrical parameter C is introduced for chiral helicoidal particles in [28] This shape constant, now termed as the Ishimoto parameter [39], characterises the level of chirality and is useful to study bacterial motility in flow [31, 38] More generally, optimisation of entries the mobility tensor, which is defined as the inverse of the resistance tensor, may be relevant in swimming-related applications.

Beyond these refinements, several natural extensions emerge from our study. First, a quantitative characterisation of the objective landscape, e.g. the number and depth of local minima and the curvature around optima, would help assess the stability of computed designs and motivate multi-start strategies. Second, deriving explicit necessary optimality conditions on the boundary (from the shape derivative) would supply analytical checks for the numerically obtained candidates. These directions suggest concrete paths for future analytical and computational work.

Finally, various refinements of the Stokes problem 2.3 can be fathomed to address other open problems in microhydrodynamics and microswimming, in the lines of recent literature on the topic [6, 21, 35]. Dirichlet boundary conditions on the object surface, considered in this paper as well as in a vast part of the literature, may fail to properly describe the fluid friction arising at small scale, notably when dealing with complex biological surfaces. Nonstandard boundary conditions such as the Navier conditions [4] are then warranted. Interestingly, the optimal drag problem for a rigid body, although well resolved since long for Dirichlet conditions [42], is still open for Navier conditions.

Seeking to further connect shape optimisation to efficient swimming at microscale, one could also include some level of deformability of the object, which requires to couple the Stokes equation with an elasticity problem. A simple model in this spirit was recently introduced in the context of shape optimisation in [10]. Another problem with biological relevance it the optimisation of hydrodynamic resistance when interacting with a more or less complex environment, such as a neighbouring wall or a channel, which is known to change locomotion strategies for microorganisms [16]; overall, a dynamical, environment-sensitive shape optimisation study stemming from this paper's framework could provide key insights on microswimming and microrobot design.

Acknowledgments

C.M. acknowledges support by the PULSAR Programme from Région Pays de la Loire, and the JSPS (Postdoctoral Fellowship No. P22023 and JSPS-KAKENHI Grant-in Aid for JSPS Fellows No. 22F22023). C.M. and K.I. acknowledge support by the Research Institute for Mathematical Sciences, an International Joint Usage/Research Center located at Kyoto University. K.I. acknowledges JSPS-KAKENHI for Young Researchers (Grant No. 18K13456), JSPS-KAKENHI for Transformative Research Areas (Grant No. 21H05309), JST, PRESTO, Japan (Grant No. JPMJPR1921), and JST, FOREST, Japan (Grant No. JPMJFR212N). Y.P. was partially supported by the ANR Project Stoiques ANR-24-CE40-2216.

REFERENCES

- [1] G. Allaire, F. Jouve, A.M. Toader, Structural optimization using sensitivity analysis and a level-set method, J. Comput. Phys. 194 (2004), 363–393.
- [2] G. Allaire, Conception optimale de structures, volume 58 of Mathématiques & Applications (Berlin) [Mathematics & Applications], Springer-Verlag, Berlin, 2007.
- [3] J.M. Bourot, On the numerical computation of the optimum profile in stokes flow, J. Fluid Mech. 65 (1974), 513–515.
- [4] L. Bocquet, J.L. Barrat, Flow boundary conditions from nano- to micro-scales, Soft Matter 3 (2007), 685–693.
- [5] L. Berti, M. Binois, F. Alouges, M. Aussal, C. Prud'Homme, L. Giraldi, Shapes enhancing the propulsion of multiflagellated helical microswimmers, arXiv preprint arXiv:2103.05637, 2021.
- [6] M. Bonnet, R. Liu, S. Veerapaneni, H. Zhu, Shape optimization of peristaltic pumps transporting rigid particles in stokes flow, SIAM J. Sci. Comput. 45 (2023), B78-B106.
- [7] T. Borrvall, J. Petersson, Topology optimization of fluids in stokes flow, Int. J. Numer. Meth. Fluids 41 (2003), 77–107.
- [8] F.P. Bretherton, The motion of rigid particles in a shear flow at low reynolds number, J. Fluid Mech. 14 (1962), 284–304.
- [9] M.P. Bendsoe, O. Sigmund, Topology optimization: theory, methods, and applications, Springer, 2013.

- [10] V. Calisti, Synthesis of microstructures by topological optimization, and shape optimization of a Fluid Structure Interaction problem, PhD thesis, Université de Lorraine, 2021.
- [11] A. Courtais, A.M. Latifi, F. Lesage, Y. Privat, Shape optimization of fixed-bed reactors in process engineering, SIAM J. Appl. Math. 81 (2021), 1141–1165.
- [12] C. Dapogny, P. Frey, F. Omnès, Y. Privat, Geometrical shape optimization in fluid mechanics using FreeFem++, Struct. Multidiscip. Optim. 58 (2018), 2761–2788.
- [13] A. Daddi-Moussa-Ider, B. Nasouri, A. Vilfan, R. Golestanian, Optimal swimmers can be pullers, pushers or neutral depending on the shape, J. Fluid Mech. 922 (2021), R5.
- [14] G. Doğan, P. Morin, R. H. Nochetto, M. Verani, Discrete gradient flows for shape optimization and applications, Comput. Methods Appl. Mech. Engrg. 196 (2007), 3898–3914.
- [15] M.C. Delfour, J.P. Zolésio, Shapes and Geometries: Metrics, Analysis, Differential Calculus, and Optimization, SIAM, 2011.
- [16] J. Elgeti, G. Gompper, Microswimmers near surfaces, Eur. Phys. J. Special Topics, 225 (2016), 2333–2352.
- [17] A. Evgrafov, Topology optimization of slightly compressible fluids, J. Appl. Math. Mech. 86 (2006), 46–62.
- [18] T. Fujita, T. Kawai, Optimum shape of a flagellated microorganism, JSME International Journal Series C Mechanical Systems, Machine Elements and Manufacturing 44 (2001), 952–957.
- [19] G. P. Galdi, An introduction to the mathematical theory of the Navier-Stokes equations, second edition, Springer Monographs in Mathematics, Springer, New York, 2011.
- [20] M.D. Gunzburger, H. Kim, Existence of an optimal solution of a shape control problem for the stationary navier–stokes equations, SIAM J. Control Optim. 36 (1998), 895–909.
- [21] H. Guo, H. Zhu, R. Liu, M. Bonnet, S. Veerapaneni, Optimal ciliary locomotion of axisymmetric microswimmers, J. Fluid Mech. 927 (2021), A22.
- [22] A. Henrot, Shape Optimization and Spectral Theory, De Gruyter, Berlin, 2017.
- [23] J. Haslinger, R.A.E. Mäkinen, Introduction to Shape Optimization: Theory, Approximation, and Computation, SIAM, 2003.
- [24] A. Henrot, I. Mazari-Fouquer, Y. Privat, Is the faber–krahn inequality true for the stokes operator? Calc. Var. Partial Differential Equations 63 (2024), 228.
- [25] A. Henrot, Y. Privat, What is the optimal shape of a pipe? Arch. Ration. Mech. Anal. 196 (2010), 281–302.
- [26] A. Henrot, M. Pierre, Shape variation and optimization, volume 28 of EMS Tracts in Mathematics, European Mathematical Society (EMS), Zürich, 2018.
- [27] K. Ishimoto, Hydrodynamic evolution of sperm swimming: Optimal flagella by a genetic algorithm, J. Theoret. Biol. 399 (2016), 166–174.
- [28] K. Ishimoto, Helicoidal particles and swimmers in a flow at low reynolds number, J. Fluid Mech. 892 (2020), A11
- [29] K. Ishimoto, Jeffery orbits for an object with discrete rotational symmetry, Phys. Fluids 32 (2020), 081904.
- [30] G. B. Jeffery, The motion of ellipsoidal particles immersed in a viscous fluid, Proceedings of the Royal Society A: Mathematical, Physical and Engineering Sciences 102 (1922), 161–179.
- [31] G. Jing, A. Zöttl, E. Clément, A. Lindner, Chirality-induced bacterial rheotaxis in bulk shear flows Sci. Adv. 6 (2020), eabb2012.
- [32] S. Kim, S.J. Karrila, Microhydrodynamics: Principles and Selected Applications, Butterworth Heinemann Series in Chemical Engineering. Dover Publications, 2005.
- [33] E.E. Keaveny, S.W. Walker, M.J. Shelley, Optimization of chiral structures for microscale propulsion, Nano lett. 13 (2013), 531–537.
- [34] E. Lauga, The Fluid Dynamics of Cell Motility, vol. 62, Cambridge University Press, Cambridge, 2020.
- [35] R. Liu, H. Zhu, H. Guo, M. Bonnet, S. Veerapaneni, Shape optimization of slip-driven axisymmetric microswimmers, SIAM J. Sci. Comput. 47 (2025), A1065–A1090.
- [36] T.D. Montenegro-Johnson, E. Lauga, The other optimal stokes drag profile, J. Fluid Mech. 762 (2015).
- [37] B. Mohammadi, O. Pironneau, Applied Shape Optimization for Fluids, second edition, Oxford University Press, Oxford, 2010.
- [38] K. Ogawa, K. Ishimoto, Generalized taylor dispersion of chiral microswimmers, Philosophical Transactions A, 383 (2025), 20240262.

- [39] T. Ohmura, Y. Nishigami, A. Taniguchi, S. Nonaka, T. Ishikawa, M. Ichikawa, Near-wall rheotaxis of the ciliate tetrahymena induced by the kinesthetic sensing of cilia, Sci. Adv. 7 (2021), eabi5878.
- [40] S. Osher, J.A. Sethian, Fronts propagating with curvature-dependent speed: algorithms based on hamilton-jacobi formulations, J. Comput. Phys. 79 (1988), 12–49.
- [41] C. Pozrikidis, et al., Boundary Integral and Singularity Methods for Linearized Viscous Flow, Cambridge University Press, Cambridge, 1992.
- [42] O. Pironneau, On optimum profiles in stokes flow, J. Fluid Mech. 59 (1973), 117–128.
- [43] C. Pozrikidis, A practical guide to boundary element methods with the software library BEMLIB, CRC Press, 2002.
- [44] E.M. Purcell, Life at low reynolds number, Amer. J. Phys. 45 (1977), 3–11.
- [45] J.E. Quispe, A. Oulmas, S. Régnier, Geometry optimization of helical swimming at low reynolds number, In: 2019 International Conference on Manipulation, Automation and Robotics at Small Scales (MARSS), pp. 1–6, IEEE, 2019.
- [46] S. Richardson, Optimum profiles in two-dimensional stokes flow, Proceedings of the Royal Society of London. Series A: Mathematical and Physical Sciences, 450 (1995), 603–622.
- [47] A. Ryabov, O. Kerimoglu, E. Litchman, I. Olenina, L. Roselli, A. Basset, E. Stanca, B. Blasius, Shape matters: the relationship between cell geometry and diversity in phytoplankton, Ecology Lett. 24 (2021), 847–861.
- [48] V. Singh, D.L. Koch, A.D. Stroock, Rigid ring-shaped particles that align in simple shear flow, J. Fluid Mech. 722 (2013), 121–158.
- [49] D.K. Srivastava, Optimum cross section profile in axisymmetric stokes flow, J. Fluids Eng. 133 (2011), 101202.
- [50] J.A. Sethian, A. Wiegmann, Structural boundary design via level set and immersed interface methods, J. Comput. Phys. 163 (2000), 489–528.
- [51] B. Velichkov, Shape optimization problems in a box, pp. 13-58. Scuola Normale Superiore, Pisa, 2015.
- [52] A. Vilfan, Optimal shapes of surface slip driven self-propelled microswimmers, Physical Rev. Lett. 109 (2012), 128105.
- [53] M.C.F. van Teeseling, M. A de Pedro, F. Cava, Determinants of bacterial morphology: from fundamentals to possibilities for antimicrobial targeting, Front. Microbiol. 8 (2017), 1264.
- [54] S.W. Walker, The shapes of things: a practical guide to differential geometry and the shape derivative, SIAM, 2015.
- [55] R.J. Wheeler, Use of chiral cell shape to ensure highly directional swimming in trypanosomes, PLoS Comput. Biol. 13 (2017), e1005353.
- [56] S.W. Walker, E.E. Keaveny, Analysis of shape optimization for magnetic microswimmers, SIAM J. Control Optim. 51 (2013), 3093–3126.
- [57] M.Y. Wang, X. Wang, D. Guo, A level set method for structural topology optimization, Comput. Meth. Appl. Mech. Eng. 192 (2003), 227–246.
- [58] D.C. Yang, K.M. Blair, N.R. Salama, Staying in shape: the impact of cell shape on bacterial survival in diverse environments, Microbiology and Molecular Biology Reviews, 80 (2016), 187–203.
- [59] M. Zabarankin, Minimum-resistance shapes in linear continuum mechanics, Proceedings of the Royal Society A: Mathematical, Physical and Engineering Sciences, 469 (2013), 20130206.